

# CAPTURING CENTIMETER-SCALE LOCAL VARIATIONS IN PAPER PORE SPACE VIA $\mu$ -CT: A BENCHMARK STUDY USING CALENDERED PAPER

MATTHIAS NEUMANN,<sup>1</sup> EDUARDO MACHADO CHARRY,<sup>2,3</sup>  
EKATERINA BAIKOVA,<sup>2,3</sup> ANDRÉ HILGER,<sup>4</sup> ULRICH HIRN,<sup>3,5</sup>  
ROBERT SCHENNACH,<sup>2,3</sup> INGO MANKE,<sup>4</sup> VOLKER SCHMIDT,<sup>1</sup> AND  
KARIN ZOJER<sup>2,3</sup>

<sup>1</sup>*Institute of Stochastics, Ulm University, Helmholtzstraße 18, 89069 Ulm, Germany*

<sup>2</sup>*Institute of Solid State Physics, NAWI Graz, Graz University of Technology, Petersgasse 16/III, 8010 Graz, Austria*

<sup>3</sup>*Christian Doppler Laboratory for mass transport through paper, Graz University of Technology, Petersgasse 16/III, 8010 Graz, Austria*

<sup>4</sup>*Institute of Applied Materials, Helmholtz-Zentrum Berlin für Materialien und Energie, Hahn-Meitner-Platz 1, 14109 Berlin*

<sup>5</sup>*Institute of Bioproducts and Paper Technology, Graz University of Technology, Inffeldgasse 23, 8010 Graz, Austria*

**ABSTRACT.** A two-step framework to analyze local microstructure variations of paper sheets based on 3D image data is presented. First, a multi-stage workflow efficiently acquires a large set of highly-resolved tomographic image data, which enables—in combination with statistical image analysis—the quantification of local variations and pairwise correlations of morphological microstructure characteristics on length scales ranging from micrometers to centimeters. Secondly, the microstructure is analyzed in terms of the local behavior of porosity, thickness, and further descriptors related to transportation paths. The power of the presented framework is demonstrated showing that it allows one (i) to quantitatively reveal the difference in terms of local structural variations between a model paper before and after unidirectional compression via hard-nip calendering, and that (ii) the field of view which is required to reliably compute the probability distributions of the considered local microstructure characteristics is at least  $20 \text{ mm}^2$ . The results elucidate structural differences related to local densification. In particular, it is shown how calendering transforms local variations in sheet thickness into marked local mass density variations. The obtained results are in line with experimental measurements of macroscopic properties (basis weight, Bekk smoothness parameters, thickness, Gurley retention times).

## 1. INTRODUCTION

X-ray microcomputed tomography ( $\mu$ -CT) is an established and indispensable tool to unveil the structure and composition of disordered and inhomogeneous materials (Kinney et al., 1988; Banhart, 2008; Stock, 2019). Despite the successful application of  $\mu$ -CT, there is a class of materials for which it is highly challenging to capture the degree of disorder and to determine the extent of microstructural heterogeneity in general. This class comprises thin sheet materials with enormous aspect ratios. Such materials occur, for example, in batteries or fuel cells, where  $\mu$ -CT was successfully used to investigate their local microstructure variations (Harris

---

*Key words and phrases.* hard-nip calendering of paper material, experimental microstructure characterization, local microstructure variation, statistical image analysis, X-ray microcomputed tomography.

& Chiu, 2015; Banerjee et al., 2016). Furthermore, thin sheet materials appear in filtering applications and even as consumer products in daily use. Paper sheets also fall in this class and illustrate well large aspect ratios, as paper features areas in square centimeters or even square meters while it is only several micrometers thin or even less. Correspondingly, possible microstructure variations manifest themselves on length scales that may span seven orders of magnitude (Chinga-Carrasco, 2009). Thus paper can be considered as a multi-scale material (Kent, 1991; Vernhes et al., 2008; Simon, 2020), particularly when variations in transversal and lateral directions are compared. The quantification of microstructure variations in both directions, *i.e.*, variations on two different length scales, is crucial to predict the macroscopic behavior of paper sheets and of thin sheet materials in general. Using  $\mu$ -CT allows for resolving features on the sub-micrometer scale. Still, it practically limits the field of view captured with a single  $\mu$ -CT scan, which is several orders of magnitude smaller than the required lateral extension. Hence it is highly desirable to explore how  $\mu$ -CT can be utilized in combination with statistical image analysis to characterize microstructures of such high aspect ratio materials, including their local variations. In the present study, we consider paper-based materials and their pore space as an elegant test bed for designing and performing a  $\mu$ -CT-based microstructure acquisition that is capable of revealing variations that laterally occur within a sheet. In general, paper materials consist of a complex network of fibers. When paper sheets form, the fibers tend to arrange into mats being one fiber thick that stack on top of each other. This forming process induces strong local variations in the microstructure of paper, which are typical for fiber-based microstructures in general (Dirrenberger et al., 2014). The microstructure, in turn, strongly influences the effective macroscopic properties of paper. Thus, a quantitative understanding of relationships between the microstructure and effective macroscopic properties, as, *e.g.*, the air permeance (Gurnagul et al., 2009), must account for these local variations.

For paper sheets, lateral mapping of locally varying properties such as thickness, basis weight, and transversally averaged mass density was already demonstrated (Dodson et al., 2001a,b; Sung et al., 2005; Sung & Keller, 2008; Keller et al., 2012). Such studies readily combine a lateral resolution as low as 100  $\mu\text{m}$  with mapped areas of 25 to 100  $\text{mm}^2$  (Keller et al., 2012). To achieve mass density maps,  $\beta$ -radiography for basis weight determination is combined with the laser profilometry for thickness mapping. Though already correlations between local thickness and basis weight can be elegantly extracted from these maps (Dodson et al., 2001a; Keller et al., 2012), it is highly desirable to also incorporate details of the pore space; for example, to establish relations between basis weight, thickness, and porosity (Dodson & Sampson., 1999).

For properties associated with the pore space of paper, the impact of local variations on the so-called floc scale is not well established so far. Flocs are regions in which the fibers tend to aggregate more strongly than in adjacent regions and are non-regularly distributed across the paper sheets. Size and separation of such flocs can continuously vary between several micrometers and centimeters. Previous studies employing  $\mu$ -CT scans intriguingly indicate that selected properties associated with the porous nature of the microstructure can be reliably captured with representative elementary volumes (REV), see Rolland du Roscoat et al. (2007, 2012), Defrenne et al. (2017) and Aslannejad & Hassanizadeh (2017). Note that besides 3D imaging, synthetic microstructures modeling paper sheets are used to quantify REV sizes (Li et al., 2018). Such an REV, as defined in Kanit et al. (2003), is the smallest volume cutout from which certain (global) microstructure descriptors can be computed with a pre-defined accuracy. This pre-defined accuracy influences the REV size, see the detailed discussion in Section 5.2 of Rolland du Roscoat et al. (2007). This means, in turn, that for a given REV size, the variability of microstructure descriptors does not completely vanish. Note that, instead of one large volume, a sufficiently large number of small volumes can be considered as representative for a given microstructure (Kanit et al., 2003). Further investigations of REV sizes in the spirit of Kanit et al. (2003) can be found, *e.g.*, in Fritzen & Boehlke (2011) for metal ceramic composites, in Stroeven et al. (2004) for granular materials, or in Wimmer et al. (2016) for asphalt concrete.

In the present study, we go beyond the investigation of REV sizes and quantify local variations of microstructure descriptors in regions, which are smaller than the REV size. Moreover, we propose a  $\mu$ -CT based workflow to acquire sufficiently large and highly resolved image data of the microstructure to incorporate the floc scale, *i.e.*, to reach out to variations that laterally occur within the sheet. For that purpose, we use model paper sheets with marked variations in the local basis weight. These variations are present not only at length scales accessible with submicrometer-resolved  $\mu$ -CT scans, but also beyond a centimeter, *i.e.*, at the floc scale. To check whether the resulting data set is large enough to capture the local variations on the floc scale, we applied our workflow to a model paper before and after hard-nip calendering. The calendering technique is abundant in paper making and compresses the paper to smooth its surfaces. In our case, we use hard-nip calendering to modify the microstructure of paper sheets and its variation in a controlled way. As the model paper contains virgin fibers without additional fillers or coating, the calendering transforms local variations of the sheet thickness into local variations of the corresponding mass density (Sung et al., 2005). Along with a local densification, the surface roughness is also reduced. This is an effect, which has been elucidated in Sampson & Wang (2020) based on theoretical considerations and supported by a data-based validation. Regions notably rich in fibers (flocs) are densified, while regions with fewer fibers (*i.e.*, regions with a small local thickness) remain practically unchanged. Hence, calendering is expected to cause changes regarding local variations of pore-space related properties. If the image data obtained by  $\mu$ -CT and related to the uncompressed and compressed paper is sufficiently comprehensive, we should be able to reveal and explain the impact of the transition on the local porosity, thickness, and pathways through the pore space. Thus, based on our previously published approach for the statistical analysis of local variations in the microstructure of paper materials (Neumann et al., 2021), we will quantify the local variations of porosity and path length related descriptors as well as the correlation between these quantities. Moreover, in the present study, we will also take into account an additional structural descriptor, namely the local thickness of the considered paper sheets.

The remaining part of the present article is structured as follows: First, we give a methodological overview, which includes descriptions of the materials and experimental measurements, the workflow to efficiently perform  $\mu$ -CT scans for providing a comprehensive set of image data representing the microstructure, and a description of the methods used for statistical image analysis. Second, we quantify the influence on the paper materials induced by compression. We present results regarding experimentally determined macroscopic characteristics and results regarding changes in the microstructure obtained by statistical image analysis. In particular, methods of statistical image analysis are used to reveal whether the changes in the microstructure due to local compressions can be unambiguously identified and explained. This is done on the basis of analyzing the (univariate) distribution of local structural descriptors of the pore space and of pairwise correlations between them. Moreover, we scrutinize the representativity of our data sets, *i.e.*, we analyze the dependence of our results on the size of image data.

## 2. MATERIALS AND METHODS

**2.1. Material and experimental characterization.** As a model system for our investigations, we consider the same paper material before and after compression. As an uncompressed reference material, we use a commercial, unbleached paper with a specific basis weight of 100 g/m<sup>2</sup>. This value, which corresponds to the supplier specifications, was confirmed by a test in accordance to the corresponding ISO standard (ISO 536:2019, 2019). The paper consists of virgin fibers, does not contain intentional fillers, and has not passed any mechanical post-treatment. During the forming of such a paper, any local accumulation of fibers (flocs) leads to thickness variations in the sheet. Though these thickness variations are induced by local variations in the basis weight, the local mass density ought to show small deviations only. For obtaining compressed samples, several sheets of the reference paper were subjected to a hard-nip, steel-steel calendering with a line load of 90 N/m.

Each paper type underwent a basis characterization in terms of basis weight, caliper-based thickness, smoothness and air retention times. The local basis weight was determined using  $\beta$ -radiography as described in (Kritzinger et al., 2008). Note that smoothness and retention times have been determined with the Bekk method (ISO 5627:1995, 1995) and the Gurley method (ISO 5636-5:2013, 2013), respectively.

**2.2. Workflow to acquire large  $\mu$ -CT data sets.** 3D imaging via  $\mu$ -CT is an established method to explore the pore space of paper (Rolland du Roscoat et al., 2007, 2012; Defrenne et al., 2017; Aslannejad & Hassanizadeh, 2017). When focussing on the pore space, the large spread of pore sizes requires a particular balanced trade-off between resolution and field of view, *i.e.*, the sample size. A high resolution aids to reveal smaller pores with diameters in the range of  $1\ \mu\text{m}$ . Such an appropriate voxel resolution of  $0.7\ \mu\text{m}$  permits to scan a volume of *ca.*  $2\ \text{mm}^2 \times \text{thickness}$ .

In such small volumes, it is challenging to capture a representative amount of larger pores with diameters in the order of  $50\ \mu\text{m}$  and beyond. The above mentioned sample volume of *ca.*  $2\ \text{mm}^2 \times \text{thickness}$  is particularly small in comparison to fields of view in the  $1\text{-}10\ \text{cm}^2$  range that are considered to capture local variations including the floc scale (Sampson, 2001). To explore the microstructure of paper materials beyond these small volumes without sacrificing resolution, multiple sample volumes stemming from different positions of the paper sheet have to be measured (Rolland du Roscoat et al., 2012; Defrenne et al., 2017; Aslannejad & Hassanizadeh, 2017).

A large number of scans implies an enormous effort when the currently prevalent  $\mu$ -CT setup for paper is employed (Rolland du Roscoat et al., 2007, 2012; Defrenne et al., 2017; Aslannejad & Hassanizadeh, 2017; Machado Charry et al., 2018). Moreover, the latter scanning setups can be considered as inherently inefficient. The effort and lack of efficiency are readily spotted when inspecting prevalent setups more closely. During scanning by  $\mu$ -CT, samples are attached to the sample holder to prevent any motion during scans or rotations. The measurement aims at collecting projections of the sample at different rotation angles. These rotations occur with respect to the vertical axis. If the paper would move during the scan, features which become involuntarily displaced in the projections would lead to a loss in resolution of the reconstructed 3D image. Paper samples are usually attached to the sample holder in an upright standing position. The upright position orients the paper perpendicular to the X-ray beam such that the beam hits the largest possible cross-sectional area for each rotational angle. However, regardless of the orientation to the beam, the sample volume fills only a small fraction of the actually scanned volume due to its particularly high area-to-thickness aspect ratio.

In the following, we propose a workflow related to sample preparation and scanning, that holds the promise to reduce the effort associated to scan multiple volumes, enhances the efficiency of each scan, and suppresses possible motion of paper samples. The key idea is to prepare samples in a multilayer configuration inspired by Schröder et al. (2016), shown in Figure 1. Several paper strips of  $10\ \text{cm} \times 1.7\ \text{mm}$  were cut from a paper sheet with the laser cutter. The latter technique allows not only for a precise control of the strips extension and uniformity, it also keeps the regions affected by cutting at a minimum. Two long strips of paper were stacked and folded in the center. Kapton strips were inserted between the layers and the resulting stack was put into a Kapton tube. Kapton is a polyimide thin film that is transparent for X-rays, *i.e.*, it does not contribute to absorption contrast. The diameter of the tube is chosen to exactly fit the diameter of the X-ray beam, such that the cross-section of the beam is optimally exploited regardless of the rotation angle of the sample. The intercalated Kapton layers prevent the paper strips to touch each other. Furthermore, these layers and the tube wall immobilize the paper strips by preventing slipping or bending. The final configuration, see Figure 1(a), poses several benefits:

- A single scan results in several virtual volumes at once, which enables us to overcome the inefficiency of scanning stand-alone paper samples.

- The paper stack is sufficiently immobilized in the tube, thus avoiding the use of a non-intrusive yet X-ray-stable adhesive.
- By moving the content of the tube along the main vertical axis, additional scans can be readily obtained without the need of time-consuming sample changes.
- It is possible to overlap consecutive scans, which allows us to create larger virtual volumes.

It is worth pointing out that this sample preparation also enables us to keep the registration of the scanned volume with respect to the paper sheet (Figure 1e). This, in turn, allows us to (i) relate the orientation of the reconstructed 3D images to the machine and cross-direction and (ii) to deliberately pick and compare regions from the paper sheet.

We successfully employed this sample setup at two synchrotron radiation  $\mu$ -CT facilities. The uncompressed paper samples were imaged in absorption mode with an energy of 20 keV, at the TOMCAT beamline (Stampanoni et al., 2007) of the Swiss Light Source at the Paul Scherrer Institute. For this purpose, a CMOS camera (pco.edge,  $2560 \times 2160$  pixel) with a magnification of 10 was used. This leads to a field of view of  $1.7 \times 1.4$  mm<sup>2</sup> and a final voxel size of  $0.65$   $\mu$ m, where 1501 projections were recorded over an angular range of  $180^\circ$  with an exposure time of 250 ms. The tomographic reconstructions were performed by means of the Gridrec algorithm (Marone & Stampanoni, 2012). In total, 150 volumes were obtained in 27 scans that covered a totally scanned area of *ca.* 2.9 cm<sup>2</sup> (Figure 1). Note that for those 27 scans, the measurements were performed with a different number of samples per scan. More precisely, 22 scans were obtained with 6 samples per scan, 4 scans with 4 samples, and 2 scans with one sample. The compressed samples were imaged in inline phase contrast mode at P05 beamline of the PETRA III storage-ring at DESY in Hamburg (Wilde et al., 2016; Haibel et al., 2010). The synchrotron beam was generated with an undulator and monochromatized with a double crystal monochromator to an energy of 20 keV. After transmitting the sample, the monochromatic X-rays were transformed into visible light using a CdWO<sub>4</sub> scintillator. The optical lens system in combination with a CMOS camera (KIT CMOS,  $5120 \times 3840$  pixel) covered a field of view of  $3.29 \times 2.46$  mm<sup>2</sup>. The resulting pixel size of the system was  $0.64$   $\mu$ m, where 2400 projections were recorded over an angular range of  $180^\circ$  with an exposure time of 60 ms. Furthermore, four samples were measured in each scan with a distance of 40 mm between sample and scintillator. For the tomographic reconstruction of the sample, the MabATLAB based (The MathWorks, USA) library Astra Toolbox (Van Aarle et al., 2015, 2016) was used. In total, we obtained 52 volumes in 13 scans. For these volumes, a two times binning was used to give a resulting voxel size of  $1.3$   $\mu$ m.

Figure 2 shows 2D slices of the greyscale images representing the microstructure of the considered uncompressed and compressed paper materials. Here one can observe that the differently performed measurements lead to different types of contrast, which, in turn, require different methods for segmentation, *i.e.*, for the classification of individual voxels as cellulose material or its complementary void space. While the contrast in the images showing the uncompressed paper sheets allows for a segmentation based on absorption contrast by means of indicator kriging (Oh & Lindquist, 1999) as in Machado Charry et al. (2018), this is not possible for the image data representing the compressed paper sheets. In the latter case, the absorption contrast between cellulose and void space is low. However, a clear phase contrast at the boundary of the cellulose allows for a segmentation using a random forest classifier within the FIJI Weka Segmentation plugin (Schindelin et al., 2012; Arganda-Carreras et al., 2017). For resolving the pore structure and the thickness, we determined top and bottom surfaces of the binarized volumes with the rolling ball approach (Sternberg, 1983) that has already been used for 3D image data of paper materials (Svensson & Aronsson, 2003; Sintorn et al., 2005; Chinga-Carrasco et al., 2008; Machado Charry et al., 2018) and battery electrodes (Kuchler et al., 2018). For the present study, we re-binned the image data of the uncompressed sample such that the voxel sizes of both samples coincide. Doing so, we ensure that the results from statistical image analysis are comparable to each other.

**2.3. Statistical image analysis.** Using methods of spatial statistics (Ohser and Schladitz, 2013; Chiu et al., 2013), we quantify local variations in the uncompressed and compressed paper sheets. For this purpose, we determine spatially resolved microstructure descriptors by partitioning all binarized data sets into non-overlapping cutouts. These cutouts, which serve as local inspection regions, are square-shaped in lateral direction and contain the entire thickness of the paper sheet as described in Neumann et al. (2021). The side length of the squares is varied between 30  $\mu\text{m}$  and 330  $\mu\text{m}$ . In total, for statistical image analysis, we take 306 and 352 cutouts in the uncompressed and compressed case into account, respectively. This means that in both cases, we use an area of more than 30  $\text{mm}^2$  for our analysis. As microstructure descriptors, we consider spatially resolved thicknesses, porosities, and mean geodesic tortuosities. Note that the mean geodesic tortuosity  $\tau_0$  quantifies the length of shortest transportation paths through the pore space. More precisely, for a given cutout, we compute the mean value of the length of shortest transportation paths going from the inner surface of the paper sheet intersected with this cutout through the pore space to the outer surface of the sheet. Then,  $\tau_0$  is defined as this mean value divided by the local thickness of the sheet. For further details regarding mean geodesic tortuosity, we refer to Stenzel et al. (2016) and Neumann et al. (2019). In general, for  $r > 0$ , the descriptor  $\tau_r$  is analogously defined (Neumann et al., 2021), but only paths which can be passed by balls of radius  $r$  (in  $\mu\text{m}$ ) are taken into account. In this study, we particularly consider  $\tau_0$  and  $\tau_{3.0}$ . The statistical analysis of local microstructure descriptors provides the variability of local thicknesses, local porosities, and the local tortuosities  $\tau_0$  and  $\tau_{3.0}$  for paper sheets before and after compression. The pairwise interdependence between local porosities and both, local tortuosities as well as local thicknesses, are quantified by means of correlation coefficients.

### 3. RESULTS

**3.1. Changes in macroscopic properties.** To begin with, we consider macroscopic properties of the samples before and after compression in order to quantify the compression-induced changes. The experimentally measured values are shown in Figure 3. This figure comprises the values of the basis weight, the caliper-based thickness, the Bekk smoothness parameter, and the Gurley retention time.

The basis weight measured (at two different locations) for the samples before and after compression stays essentially the same at *ca.* 100  $\text{g}/\text{m}^2$ , see Figure 3(a). The variation of the basis weight was assessed by inspecting the power spectra of the  $\beta$ -radiographs (Norman and Wahren, 1974) with a size of  $10 \times 10 \text{ cm}^2$ . The radiograph of the uncompressed sample is exemplarily shown in Figure 1(e); all further  $\beta$ -radiographs and the related power spectra are provided as supplementary material. The power spectra reveal a larger variation in the compressed sample across all length scales between 0.2 mm and 2 cm. Below 1.2 mm, *i.e.*, on length scales observable within the field of view of  $\mu$ -CT scans, the variation is only subtly enhanced after calendering. This implies that calendering did not strictly preserve the local mass density, but did not profoundly alter the lateral fiber arrangement either.

The smoothness of surfaces is characterized using the Bekk method. The Bekk smoothness parameter informs on the time (in seconds) for a fixed volume of air to leak between the surfaces of a paper sample and a smooth glass. According to Figure 3(c), the Bekk smoothness parameters associated to top and bottom surface strongly increase after calendering, which is in line with the intended purpose of calendering. Remarkably, the variation of the smoothness parameters increases with calendering as well. Formerly dominating air-leakage pathways permitting large volume fluxes are likely replaced by a large variety of leakage pathways carrying considerably less air volumes. The caliper-based thickness (Figure 3(b)), *i.e.*, the apparent thickness associated with the most protruding regions of the paper sheets, shows a marked reduction after compression from 141 to 108  $\mu\text{m}$ . Also the measured variation of thickness reduces due to the surface smoothing.

The Gurley retention time shown in Figure 3(d) is inversely proportional to the volume flux of air that each of the two paper samples permit. Regardless whether air is transported from the top to bottom surface (side 1 in Figure 3) or vice versa (side 2 in Figure 3), compression leads to a twice as high retention time and a marked enhancement in variation. The corresponding decrease in volume flux indicates a substantial change in the pore space available for air transport.

**3.2. Local changes of the microstructure.** To relate this profound reduction in volume flux to local properties of the pore-space, we turn to the inspection of the microstructure. Illustrative cutouts taken from the 3D microstructure of each of the two paper samples are shown in Figure 4(a,b) and emphasize the most striking differences between them. The uncompressed sample shows a marked corrugation of the surface that is, at least in part, caused by a spatially fluctuating number of vertically stacked fibers (black regions in Figure 4(a)). Correspondingly, less fibers lead to a reduced local thickness  $\delta$  in that region, as illustrated in Figure 4(c). In contrast, the compressed sample shows rather smooth surfaces and an apparently constant and overall reduced thickness. Beyond thickness reduction and smoothing, hard-nip calendering is expected to compact the paper transversely such that the most protruding fiber-rich regions are compacted in vertical direction. The less a feature protrudes beyond the final thickness, the less the paper is locally compacted. The microstructure of regions, in which fibers do even not protrude at all, are essentially preserved. In this way calendering transforms regions of different thicknesses into regions of different degrees of compression and, thus, of different mass densities. Figure 4(d) illustrates that this compression acts locally. Depending on the location, the sample is compressed to a fraction of the original thickness of the sample. Some regions are not compressed at all and hence preserve their original thickness and structure. Turning back to the cross-section of the compressed sample shown in Figure 4(b), we may indeed discern between regions with a high density of fibers (indicated in black) related to a marked compression and regions with a lower density of fibers, representing small if not even absent compression. To substantiate these observations, we perform statistical image analysis where the focus is on four selected, local microstructure descriptors which have been introduced above: Thickness, porosity, mean geodesic tortuosity,  $\tau_0$ , related to all pathways, and mean geodesic tortuosity,  $\tau_{3,0}$ , associated to high volume pathways exhibiting a minimum diameter of  $3 \mu m$ . This image analysis provides (i) the univariate distributions of these quantities, (ii) the pairwise interdependence between them, and (iii) their dependence on the number and size of the local inspection regions. While the former two quantitatively assess the impact of calendering, the latter will inform us, whether the data set has been representative for the paper sheet.

Figure 5 compares the univariate distributions of the selected local quantities in terms of the probability density functions for cutout sizes of  $90 \mu m$  and  $330 \mu m$ . Each panel displays the distribution for the uncompressed sample in the upper half and the corresponding distribution for the compressed sample in the lower half. Note that we determined the probability density functions by diffusion-based kernel density estimation (Botev et al., 2010). A first inspection suggests that calendering-induced profound changes in the local thickness, local porosity, and in  $\tau_{3,0}$ . To quantify the interdependence between the local microstructure descriptors we determined the correlation coefficients between path-length related descriptors and local porosity as well as local thickness. This set of correlation coefficients, shown as functions of the cutout size in Figure 6, suggest a marked difference in the microstructures.

However, before inspecting the differences between the paper samples revealed by univariate distributions and correlation coefficients more closely (as will be done in the following section), it is important to evaluate first whether the estimated local distributions are representative for the samples. This is a crucial aspect, since, in case that the number of local inspection regions used for our statistical image analysis is too low, we may, *e.g.*, miss regions of pronounced fiber aggregation or regions in which fibers are particularly loosely packed. Therefore the obtained statistical results might be biased by the location of the inspection regions. We test

the requirement of considering sufficiently many local inspection regions. For this purpose, the discrepancy between the distributions computed with all cutouts and the distributions computed with a subset of all cutouts, *i.e.*, 306 cutouts for the uncompressed sample and 324 for the compressed sample, is determined. For this purpose, we consider a fixed cutout size of  $330\ \mu\text{m}$ . The results are shown in Figure 7, where the discrepancy is measured in terms of the Kolmogorov distance. Note that the Kolmogorov distance between two probability distributions is defined as the supremum distance of the corresponding cumulative distribution functions. In Neumann et al. (2021), we used the Kolmogorov-Smirnov test based on the Kolmogorov distance to validate a parametric model for the joint distribution of local porosity and local path-length related descriptors. Figure 7 shows that for all microstructure descriptors, a number of at least 200 cutouts has to be considered such that the Kolmogorov distance is below 0.05. Due to the increasing variability of local microstructure descriptors with decreasing cutout size, this statement remains valid for cutout sizes below  $330\ \mu\text{m}$ . Moreover, we provide .gif-files as supplementary material showing the evolution of the univariate distribution of each descriptor, when—step by step—more local inspection regions are incorporated until all available cutouts are used in the end. The corresponding file names are listed in Table 1.

Not only the number, but also the size of the cutouts is expected to have an impact on the univariate distributions of local microstructure descriptors. For example, Sampson (2001) illustrated that the variance in local basis weight decreases with cutout size. For all four local descriptors, considered in the present article, the mean values in dependence of the cutout size are shown in Figure 8, where the 0.95- and 0.05-quantiles are additionally given for quantifying the variability. The complete univariate distributions are provided as supplementary material.

## 4. DISCUSSION

**4.1. Distributions of local microstructure descriptors.** The univariate distributions of local microstructure characteristics reveal profound differences between the two samples: The distributions of local thicknesses (Figure 5(a,e)) and local porosities (Figure 5(b,f)) fully corroborate the expected impact of calendering (Chinga et al., 2007; Vernhes et al., 2010). The probability density function of the local thickness takes its maximum at *ca.*  $110\ \mu\text{m}$  for the uncompressed sample and at *ca.*  $100\ \mu\text{m}$  for the compressed sample, respectively. Beyond that, however, the probability density function of the compressed sample sharply decreases after the maximum value. In other words, the local thicknesses do not exceed  $120\ \mu\text{m}$  after compression. However, note that—interestingly—variations towards smaller values of the local thickness behave similar for the compressed and uncompressed case (compare also Figure 8(b)). This markedly changed variability of the local thickness is fully in line with the caliper-based thickness probing and with the visual inspection of the cutouts in Figure 4(a,b). In terms of local porosity, compression causes a decrease of mean local porosity from 0.43 to 0.34. The slightly skewed distribution in Figure 5(f) suggests that the pores are not uniformly compressed. A glance on the pores found in the cutouts, shown as gray regions in Figure 4(a,b), suggests that, in particular, large pores undergo a disproportionately large compression.

Besides porosity, also the length and thickness of pathways through the pores, *i.e.*, the sinuosity and capacity of pathways, are expected to affect the volume flux of air and, hence, the Gurley retention time. We expect that calendering introduces changes in location, length, and thickness of local pathways, which affects the morphology of transportation paths as follows. First, in average, the paths—all paths as well as paths exhibiting a diameter of at least  $3\ \mu\text{m}$ —become longer. Second, the variability of the lengths of transportation paths is increased. Three major reasons lead to these assumptions: (i) The practically unchanged regions will pertain their local tortuosities; (ii) for the other regions, the following two complementary (limiting) cases suggest that the tortuosity ought to increase due to local compression. When, for example, hypothetically assuming a uniform transversal compression of pore space and fibers alike, the length of established pathways can be shown to shrink less than (or equally as) the local paper thickness. Then, the mean geodesic tortuosity increases with increasing degree of compression.

When, however, rather assuming an exclusive transversal compression of the pore space, *i.e.*, assuming rigid fibers, the local porosity shrinks. In this case, additionally to the afore-mentioned mechanism, the topology of the pore space is not necessarily preserved either, *e.g.*, because fibers getting in contact may block pathways. Then, the tortuosity rises due to the known negative correlation between porosity and tortuosity (Neumann et al., 2021). Our assumption regarding the increased local variations of the length of transportation paths is based on a third argument. Namely, (iii) as calendering introduces regions of different degrees of compression, compare the arguments (i) and (ii) mentioned above, the local variations in tortuosity and the overall mean geodesic tortuosity are expected to increase.

The distributions of  $\tau_0$  associated with all pathways (Figure 5(c,g)) do not suggest marked changes under compression. Compression changes the sample-averaged value of  $\tau_0$  merely from 1.64 to 1.63 and induces a bit more skewed distribution as well as a slightly reduced variance of  $\tau_0$ . In stark contrast to this, the descriptor  $\tau_{3,0}$  related to high-volume pathways is strongly affected by compression (Figure 5(d,h)). Compression leads to a profound increase of high-volume path lengths. The sample-average of  $\tau_{3,0}$  increases almost by a factor of two from 3.08 to 5.94 for the largest cutout-size of 330  $\mu m$ . The sample-variance of the path lengths increases even more impressively, as path lengths exceeding the local thickness by more than a factor of ten non-negligibly contribute to the distribution of  $\tau_{3,0}$ . This implies that an overwhelming fraction of the pathways is oriented parallel to the paper surface. Considering a mean local paper thickness of *ca.* 100  $\mu m$ , there are pathways spanning lateral distances of more than one millimeter.

**4.2. Pairwise interdependence between local descriptors.** With the insights gained above, we now rationalize the similarities and differences regarding the pairwise interdependence between local microstructure descriptors, which were found for the uncompressed and compressed paper. At first, we focus on the correlation coefficients between path-length related descriptors and local porosity. Note that the correlation coefficients between local porosity and both path-length related descriptors,  $\tau_0$  and  $\tau_{3,0}$ , are negative (Figure 6(a,b)) as expected in general for any porous material. With the growing size of the cutout, which is used as an inspection region, the correlation coefficient decreases for the uncompressed sample and stabilizes for large cutout sizes. This confirms the hypothesis conjectured based on maximum cutout sizes of 150  $\mu m$  in (Neumann et al., 2021), where a detailed discussion about the influence of the cutout size on the interdependence between local porosity and local path-length related descriptors is provided, see Section 4 of (Neumann et al., 2021). The stronger variation of local microstructure descriptors induced by compression might be the reason that the correlation coefficients between local porosity and  $\tau_{3,0}$  are still slightly fluctuating for large cutout sizes of the compressed sample (Figure 6(b)). Remarkably, the absolute values of correlation coefficients decrease strongly after compression. This effect is stronger for  $\tau_0$ , where the correlation is nearly vanishing, compared to the results obtained for  $\tau_{3,0}$ . Recall that we observed only small changes in the univariate distribution of  $\tau_0$ , see Figure 5. In combination with the low correlation between local porosity and  $\tau_0$ , this suggests that—after compression—the topology of pathways remains nearly unchanged, while the porosity is reduced. This also explains that the negative correlation between local porosity and  $\tau_{3,0}$  is stronger for the compressed compared to the uncompressed sample, since, by definition, more pores are required for the high-volume paths. The most critical condition to form such high-volume pathways is the ability to form an appropriately sized *vertical* connection between the fiber sheets (Sampson, 2003; Sampson & Urquhart, 2008). These findings suggest that the doubling of Gurley retention times upon calendering is caused, at least in part, by a marked reduction in porosity and by a reduction of transversal pore connections in high-volume pathways.

Moreover, we analyze the correlation coefficients between local thickness and path-length related descriptors. The results are shown in the lower panels of Figure 6, where one can observe a negative correlation between local thickness and path-length related descriptors. This means that—in average— $\tau_0$  and  $\tau_{3,0}$  decrease with increasing thickness. An exception is  $\tau_{3,0}$  in

the compressed sample, where almost no correlation is observed. Before we discuss these results in detail, recall the results of Figure 5 showing that the local thickness variation is strongly reduced upon calendaring. When considering all paths, *i.e.*, the descriptor  $\tau_0$ , the correlation coefficients before and after compression are almost indiscernible (Figure 6(c)). The reason for this might be a combination of two effects. First, as also suggested by the univariate distributions and by the correlation coefficients between local porosity and  $\tau_0$ , the topology of pathways remains unchanged after compression. Second, the impact induced by changes of local porosity is compensated by changes of the local thickness. Turning from  $\tau_0$  to  $\tau_{3.0}$ , the negative correlation becomes slightly less pronounced before compression and vanishes after compression (Figure 6(d)). Note that for the computation of path-length related descriptors of a given cutout, we consider those paths, the starting point of which is located within the cutout. However, the paths themselves might leave the cutout. Our results have shown that the high-volume paths (normalized by the local thickness) become longer after compression. This means that these paths will leave the cutout in which they start with high probability and thus the absolute values of the correlation coefficients between the local thickness and  $\tau_{3.0}$  are negligibly small. We conjecture that the small deviations of the correlation coefficient around zero are artifacts of the estimation.

**4.3. Influence of local inspection regions.** The discussion, provided above, shows that our statistical analysis allows us to unambiguously discriminate between the two paper samples. In this section, we address the influence of number and size of local inspection regions with an emphasis on the representativeness of data used in the present study. First, we show that the number of cutouts is chosen sufficiently large, to reliably determine the univariate distributions of local descriptors. In a second step, we discuss the influence of the cutout size, *i.e.*, the size of the local inspection regions, on these univariate distributions.

The results presented in Figure 7 as well as the evolution of univariate distributions, estimated from an increasing amount of data (Table 1), show that—regardless of the sample (before or after compression) and regardless of the considered local descriptor—at least 200 cutouts were necessary for a reliable estimation of the corresponding univariate distributions. We observe that the local thickness appears to be especially sensitive to the actual location of the cutouts the distribution is composed of. This observation underlines that our tomographic measurements probed indeed distinct regions. Moreover, we can conclude that for a reliable quantification of local variations based on statistical image analysis as performed in the present study, we require highly resolved image data representing an area of least  $200 \times (330\mu m)^2 = 21.78 \text{ mm}^2$ . The close relationship between effective macroscopic properties and geometrical microstructure characteristics in general (Torquato, 2002) and path-length related descriptors in particular (Stenzel et al., 2016; Neumann et al., 2020), let us strongly conjecture that the same size of image data is necessary to quantify local variations of macroscopic properties of the considered paper sheets, such as, *e.g.*, their air permeance. Note that the necessary number of cutouts for a reliable determination of the univariate distributions of local microstructure descriptors itself depends on the underlying microstructure. This means that the given value of  $21.78 \text{ mm}^2$  cannot be considered as a universal constant for all paper materials.

The results with respect to the influence of the size of local inspection regions on the mean values and corresponding 0.95- and 0.05-quantiles are presented in Figure 8. One can observe that the strongest decrease of the variability occurs when increasing the cutout size from  $30 \mu m$  to  $90 \mu m$ . But even if the domain of uncertainty between the considered quantiles becomes smaller with increasing cutout size, it remains relatively large for the cutout size of  $330 \mu m$ . Note that this variability of microstructure descriptors for cutout sizes of  $330 \mu m$  does not contradict the results obtained in Rolland du Roscoat et al. (2007), where REV sizes between  $200 \mu m \times 200 \mu m$  and  $330 \mu m \times 330 \mu m$  in lateral direction are determined using methods developed in Kanit et al. (2003). As already mentioned in the introduction, the microstructure characteristics computed from the REV in Rolland du Roscoat et al. (2007) still exhibit a certain variability.

## 5. CONCLUSION

Our multilayer stack configuration allows us to feasibly and efficiently obtain large microstructure datasets of paper by  $\mu$ -CT at a resolution that permits a detailed analysis of the pore space. Each scan provides multiple, virtual volumes at once. Inserting the paper stack into a Kapton tube prevents not only the use of any adhesives, but also allows us to readily scan other paper regions without changing the sample. The total area comprised by the individually scanned volumes reaches the order of square centimeters.

Applying the proposed multi-layer stack configuration to paper material before and after calendering allows us for a data-driven investigation of the sample size, which is necessary to reliably extract the distribution of local microstructure descriptors. We consider local porosity, local thickness, and local path-length related descriptors. Our main conclusion is that, for reliably quantifying local variations of the paper materials considered in the present study, an area in the order of 20 mm<sup>2</sup> is required. This supports the results of Kritzing et al. (2008), who have shown that—even if regions at different locations are considered—an area of several square millimeters is required to reliably determine the distribution of local thickness for coated paper sheets. Moreover, our results are in line with Dirrenberger et al. (2014), who have demonstrated that the analysis of fiber-based materials generally requires gigantic REVs.

Besides the issue of representativity, our study reveals quantitative insights regarding the influence of calendering on local microstructure descriptors. In particular, high volume pathways, being predominantly responsible for the volume flux of air, are strongly affected by compression. An overwhelming fraction of each of these pathways is oriented parallel to the paper surfaces. Compression suppresses the forming of appropriately sized transversal openings between the fiber sheets such that pathways must cover much larger distances prior finding a suitable transversal connection.

## ACKNOWLEDGEMENT

The authors gratefully acknowledge financial support from the Christian Doppler Research Association, Federal Ministry for Digital and Economic Affairs and the National Foundation for Research, Technology, and Development, Austria.

## REFERENCES

- Arganda-Carreras, I., Kaynig, V., Rueden, C., Eliceiri, K.W., Schindelin, J., Cardona, A. & Seung, H.S.** (2017). Trainable weka segmentation: a machine learning tool for microscopy pixel classification, *Bioinformatics* **33**, 2424–2426.
- Aslannejad, H. & Hassanizadeh, S.M.** (2017). Study of hydraulic properties of uncoated paper: Image analysis and pore-scale modeling, *Transport in Porous Media* **120**, 67–81.
- Banerjee, R., Hinebaugh, J., Liu, H., Yip, R., Ge, N. & Bazylak, A.** (2016). Heterogeneous porosity distributions of polymer electrolyte membrane fuel cell gas diffusion layer materials with rib-channel compression, *International Journal of Hydrogen Energy* **41**, 14885–14896.
- Banhart, J.** (ed.) (2008). *Advanced Tomographic Methods in Materials Research and Engineering*, vol. 66, Oxford: Oxford University Press.
- Botev, Z.I., Grotowski, J.F. & Kroese, D.P.** (2010). Kernel density estimation via diffusion, *The Annals of Statistics* **38**, 2916–2957.
- Chinga, G., Solheim, O. & Mörseburg, K.** (2007). Cross-sectional dimensions of fiber and pore networks based on Euclidean distance maps, *Nordic Pulp & Paper Research Journal* **22**, 500–507.
- Chinga-Carrasco, G.** (2009). Exploring the multi-scale structure of printing paper - a review of modern technology, *Journal of Microscopy* **234**, 211–242.
- Chinga-Carrasco, G., Axelsson, M., Eriksen, O. & Svensson, S.** (2008). Structural characteristics of pore networks affecting print-through, *Journal of Pulp and Paper Science* **34**, 13–22.

- Chiu, S.N., Stoyan, D., Kendall, W.S. & Mecke, J.** (2013). *Stochastic Geometry and its Applications*, Chichester: J. Wiley & Sons, 3rd ed.
- Defrenne, Y., Zhdankin, V., Ramanna, S., Ramaswamy, S. & Ramarao, B.** (2017). Three-dimensional pore structure visualization and characterization of paper using X-ray computed tomography, *Tappi Journal* **16**, 519–530.
- Dirrenberger, J., Forest, S. & Jeulin, D.** (2014). Towards gigantic RVE sizes for 3D stochastic fibrous networks, *International Journal of Solids and Structures* **51**, 359–376.
- Dodson, C.T.J. & Sampson, W.W.** (1999). Spatial Statistics of Stochastic Fiber Networks, *Journal of Statistical Physics* **96**, 447–458.
- Dodson, C.T.J., Oba, Y. & Sampson, W.W.** (2001a). Bivariate normal thickness-density structure in real near-planar stochastic fiber networks, *Journal of Statistical Physics* **102**, 345–353.
- Dodson, C.T.J., Oba, Y. & Sampson, W.W.** (2001b). On the distributions of mass, thickness and density of paper, *Appita Journal: Journal of the Technical Association of the Australian and New Zealand Pulp and Paper Industry* **54**, 385–389.
- Fritzen, F. & Boehlke, T.** (2011). Periodic three-dimensional mesh generation for particle reinforced composites with application to metal matrix composites, *International Journal of Solids and Structures* **48**, 706–718.
- Gurnagul, N., Shallhorn, P., Omholt, I. & Miles, K.** (2009). Pressurised high-consistency refining of kraft pulps for improved sack paper properties, *Appita Journal: Journal of the Technical Association of the Australian and New Zealand Pulp and Paper Industry* **62**, 25–30.
- Haibel, A., Beckmann, F., Dose, T., Herzen, J., Ogurreck, M., Müller, M. & Schreyer, A.** (2010). Latest developments in microtomography and nanotomography at PETRA III, *Powder Diffraction* **25**, 161–164.
- Harris, W.M. & Chiu, W.K.S.** (2015). Determining the representative volume element size for three-dimensional microstructural material characterization. Part 2: Application to experimental data, *Journal of Power Sources* **282**, 622–629.
- ISO 536:2019** (2019). Paper and board—determination of grammage, Standard, International Organization for Standardization, Geneva.
- ISO 5627:1995** (1995). Paper and board—determination of smoothness (Bekk method), Standard, International Organization for Standardization, Geneva.
- ISO 5636-5:2013** (2013). Paper and board—determination of air permeance (medium range)—part 5: Gurley method, Standard, International Organization for Standardization, Geneva.
- Kanit, T., Forest, S., Galliet, I., Mounoury, V. & Jeulin, D.** (2003). Determination of the size of the representative volume element for random composites: statistical and numerical approach, *International Journal of Solids and Structures* **40**, 3647–3679.
- Keller, D.S., Branca, D.L. & Kwon, O.** (2012). Characterization of nonwoven structures by spatial partitioning of local thickness and mass density, *Journal of Materials Science* **47**, 208–226.
- Kent, H.J.** (1991). The fractal dimension of paper surface topography, *Nordic Pulp & Paper Research Journal* **6**, 191–196.
- Kinney, J.H., Johnson, Q.C., Bonse, U., Nichols, M.C., Saroyan, R.A., Nusshardt, R., Pahl, R. & Brase, J.M.** (1988). Three dimensional X-ray computed tomography in materials science, *MRS Bulletin* **13**, 13–18.
- Kritzinger, J., Hirn, U., Donoser, M. & Bauer, W.** (2008). Characterization of spatial coating layer formation—definition of a representative sample size., *Proceedings of 10th TAPPI Advanced Coating Fundamentals Symposium*, 340–351.
- Kuchler, K., Prifling, B., Schmidt, D., Markötter, H., Manke, I., Bernthaler, T., Knoblauch, V. & Schmidt, V.** (2018). Analysis of the 3D microstructure of experimental cathode films for lithium-ion batteries under increasing compaction, *Journal of Microscopy* **272**, 96–110.
- Li, Y., Yu, Z., Reese, S. & Simon, J.W.** (2018). Evaluation of the out-of-plane response of fiber networks with a representative volume element model, *Tappi Journal* **17**, 329–339.

- Machado Charry, E., Neumann, M., Lahti, J., Schennach, R., Schmidt, V. & Zojer, K. (2018). Pore space extraction and characterization of sack paper using  $\mu$ -CT, *Journal of Microscopy* **272**, 35–46..
- Marone, F. & Stampanoni, M. (2012). Regridding reconstruction algorithm for real-time tomographic imaging, *Journal of Synchrotron Radiation* **19**, 1029–1037.
- Neumann, M., Hirsch, C., Staněk, J., Beneš, V. & Schmidt, V. (2019). Estimation of geodesic tortuosity and constrictivity in stationary random closed sets, *Scandinavian Journal of Statistics* **46**, 848–884.
- Neumann, M., Machado Charry, E., Zojer, K. & Schmidt, V. (2021). On variability and interdependence of local porosity and local tortuosity in porous materials: A case study for sack paper, *Methodology and Computing in Applied Probability* **23**, 613–627.
- Neumann, M., Stenzel, O., Willot, F., Holzer, L. & Schmidt, V. (2020). Quantifying the influence of microstructure on effective conductivity and permeability: virtual materials testing., *International Journal of Solid and Structures* **184**, 211–220.
- Norman, B & Wahren, D. (2020). The measurement of mass distribution in paper sheets using a beta radiographic method, *Svensk Papperstidning* **11**, 397.
- Oh, W. & Lindquist, B. (1999). Image thresholding by indicator kriging, *IEEE Transactions on Pattern Analysis and Machine Intelligence* **21**, 590–602.
- Ohser, J. & Schladitz, K. (2009). *3D Images of Materials Structures: Processing and Analysis*, Weinheim: J. Wiley & Sons.
- Rolland du Roscoat, S., Bloch, J.F. & Caulet, P. (2012). A method to quantify the 3D microstructure of fibrous materials containing mineral fillers using X-ray microtomography: application to paper materials, *Journal of Materials Science* **47**, 6517–6521.
- Rolland du Roscoat, S., Decain, M., Thibault, X., Geindreau, C. & Bloch, J.F. (2007). Estimation of microstructural properties from synchrotron X-ray microtomography and determination of the REV in paper materials, *Acta Materialia* **55**, 2841–2850.
- Sampson, W.W. (2001). The structural characterisation of fibre networks in papermaking processes - A review, C.F. Baker (ed.), *The Science of Papermaking, Transactions of the XIIIth Fundamental Research Symposium*, 1205–1288, Manchester: FRC.
- Sampson, W.W. (2003). A multiplanar model for the pore radius distribution in isotropic near-planar stochastic fibre networks, *Journal of Materials Science* **38**, 1617–1622.
- Sampson, W.W. & Urquhart, S.J. (2008). The contribution of out-of-plane pore dimensions to the pore size distribution of paper and stochastic fibrous materials, *Journal of Porous Materials* **15**, 411–417.
- Sampson, W. W, Wang, D. (2020). A model for roughness statistics of heterogeneous fibrous materials, *J. Mater. Sci.* **55**, 2636–2644.
- Schindelin, J., Arganda-Carreras, I., Frise, E., Kaynig, V., Longair, M., Pietzsch, T., Preibisch, S., Rueden, C., Saalfeld, S., Schmid, B., Tinevez, J.Y., White, D.W., Hartenstein, V., Eliceiri, K., Tomancak, P. & Cardona, A. (2012). Fiji: an open-source platform for biological-image analysis, *Nature Methods* **9**, 676.
- Schröder, D., Bender, C.L., Osenberg, M., Hilger, A., Manke, I. & Janek, J. (2016). Visualizing current-dependent morphology and distribution of discharge products in sodium-oxygen battery cathodes, *Scientific Reports* **6**, 24288.
- Simon, J.W. (2020). A review of recent trends and challenges in computational modeling of paper and paperboard at different scales, *Archives of Computational Methods in Engineering* URL (<https://doi.org/10.1007/s11831-020-09460-y>).
- Sintorn, I.M., Svensson, S., Axelsson, M. & Borgefors, G. (2005). Segmentation of individual pores in 3D paper images, *Nordic Pulp & Paper Research Journal* **20**, 316–319.
- Stampanoni, M., Groso, A., Isenegger, A., Mikuljan, G., Chen, Q., Meister, D., Lange, M., Betemps, R., Henein, S. & Abela, R. (2007). TOMCAT: A beamline for tomographic microscopy and coherent radiology experiments, *AIP Conference Proceedings*, vol. 879, 848–851, American Institute of Physics.

- Stenzel, O., Pecho, O.M., Holzer, L., Neumann, M. & Schmidt, V.** (2016). Predicting effective conductivities based on geometric microstructure characteristics, *AIChE Journal* **62**, 1834–1843.
- Sternberg, S.R.** (1983). Biomedical image processing, *Computer* **16**, 22–34.
- Stock, S.R.** (2019). *Microcomputed Tomography: Methodology and Applications*, Boca Raton: CRC Press, 2nd ed.
- Stroeven, M., Askes, H. & Sluys, L.J.** (2004). Numerical determination of representative volumes for granular materials, *Computer Methods in Applied Mechanics and Engineering* **193**, 3221–3238.
- Sung, Y.J., Ham, C.H., Kwon, O., Lee, H.L. & Keller, D.S.** (2005). Applications of thickness and apparent density mapping by laser profilometry, S.J. P Anson (ed.), *Advances in Paper Science and Technology, Transactions of the XIIIth Fundamental Research Symposium held in Cambridge*, 961–1007, Manchester: FRC.
- Sung, Y.J. & Keller, D.S.** (2008). Local Paper Structural Properties by Noncontacting Laser Profilometry, *Appita Journal: Journal of the Technical Association of the Australian and New Zealand Pulp and Paper Industry* **61**, 28.
- Svensson, S. & Aronsson, M.** (2003). Using distance transform based algorithms for extracting measures of the fiber network in volume images of paper, *IEEE Transactions on Systems, Man, and Cybernetics, Part B (Cybernetics)* **33**, 562–571.
- Torquato, S.** (2002). *Random Heterogeneous Materials: Microstructure and Macroscopic Properties*, New York: Springer.
- Van Aarle, W., Palenstijn, W.J., Cant, J., Janssens, E., Bleichrodt, F., Dabravolski, A., De Beenhouwer, J., Batenburg, K.J. & Sijbers, J.** (2016). Fast and flexible X-ray tomography using the ASTRA toolbox, *Optics Express* **24**, 25129–25147.
- Van Aarle, W., Palenstijn, W.J., De Beenhouwer, J., Altantzis, T., Bals, S., Batenburg, K.J. & Sijbers, J.** (2015). The ASTRA toolbox: A platform for advanced algorithm development in electron tomography, *Ultramicroscopy* **157**, 35–47.
- Vernhes, P., Bloch, J.F., Mercier, C., Blayo, A. & Pineaux, B.** (2008). Statistical analysis of paper surface microstructure: A multi-scale approach, *Applied Surface Science* **254**, 7431–7437.
- Vernhes, P., Dubé, M. & Bloch, J.F.** (2010). Effect of calendering on paper surface properties, *Applied Surface Science* **256**, 6923–6927.
- Wilde, F., Ogurreck, M., Greving, I., Hammel, J.U., Beckmann, F., Hipp, A., Lottermoser, L., Khokhriakov, I., Lytaev, P., Dose, T., Burmester, H., Müller, M. & Schreyer, A.** (2016). Micro-CT at the imaging beamline P05 at PETRA III, *AIP Conference Proceedings*, vol. 1741, 030035, AIP Publishing LLC.
- Wimmer, J., Stier, B., Simon, J.W. & Reese, S.** (2016). Computational homogenisation from a 3D finite element model of asphalt concrete—linear elastic computations, *Finite Elements in Analysis and Design* **110**, 43–57.

## 6. TABLES

TABLE 1. Filenames related to given geometrical descriptors in the uncompressed and compressed case

	uncompressed	compressed
porosity	porosity_movie_psi.gif	porosity_movie_hzb.gif
thickness	thickness_movie_psi.gif	thickness_movie_hzb.gif
$\tau_0$	tau0_movie_psi.gif	tau0_movie_hzb.gif
$\tau_{3.0}$	tau3_movie_psi.gif	tau3_movie_hzb.gif

## 7. FIGURES

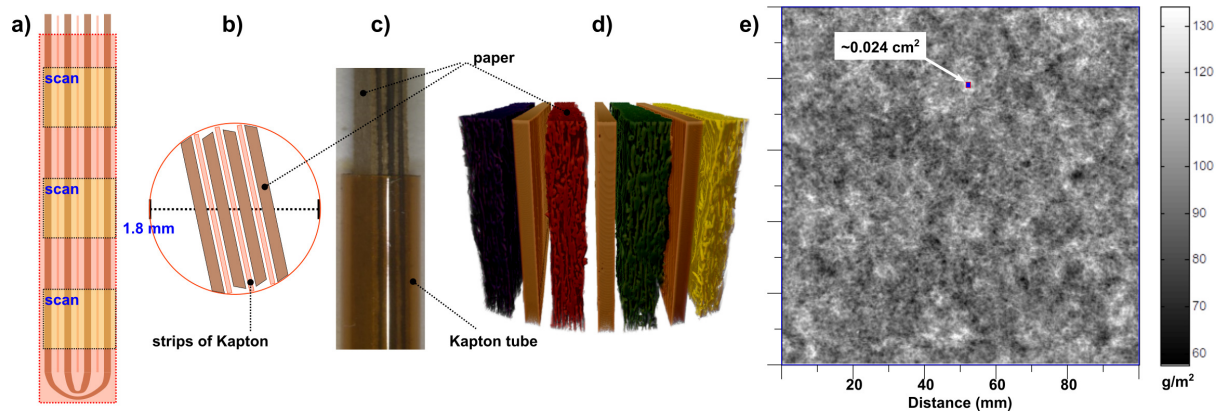


FIGURE 1. Paper strips in a Kapton tube (a-e). Overview of the paper strip alignment within the tube (a-b). Optical image showing the paper and Kapton strips inserted in the tube (c). 3D visualization of binarized image data inside the Kapton tube (d).  $\beta$ -radiograph of the uncompressed sample (e).

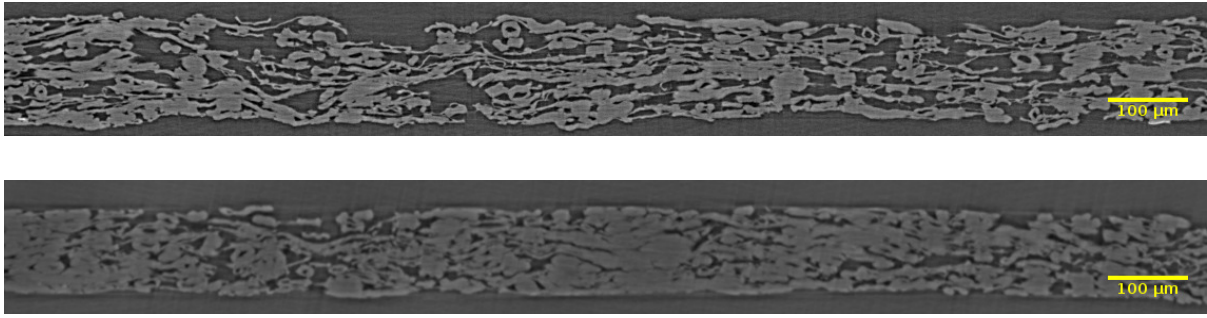


FIGURE 2. Cross-sections of greyscale images obtained by  $\mu$ -CT, which represent the microstructure of the uncompressed (top) and compressed (bottom) sample, respectively.

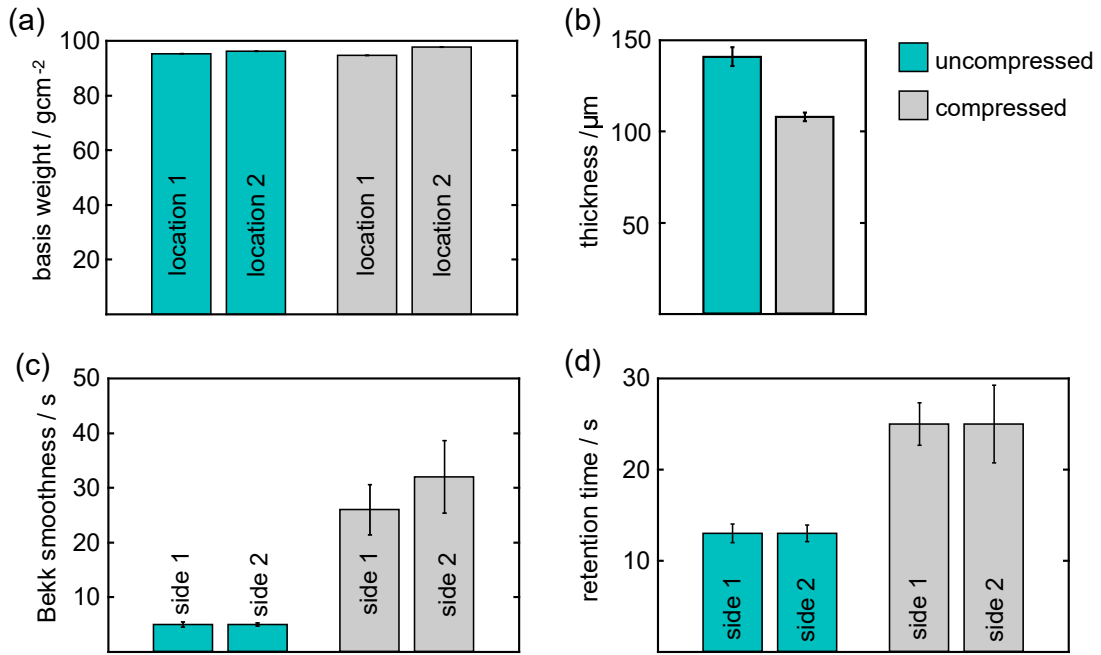


FIGURE 3. Comparison of uncompressed (blue) and compressed paper (grey) in terms of (a) basis weights (measured at two different locations), (b) caliper-based thickness, (c) Bekk smoothness parameter, and (d) Gurley retention time. The Gurley retention time and the Bekk smoothness are measured with respect to the two boundary sides of the paper sheets (side 1 and side 2 which correspond to bottom and top surface), while the basis weights are measured at two different locations of the paper sheets. The error bars show the corresponding standard deviations.

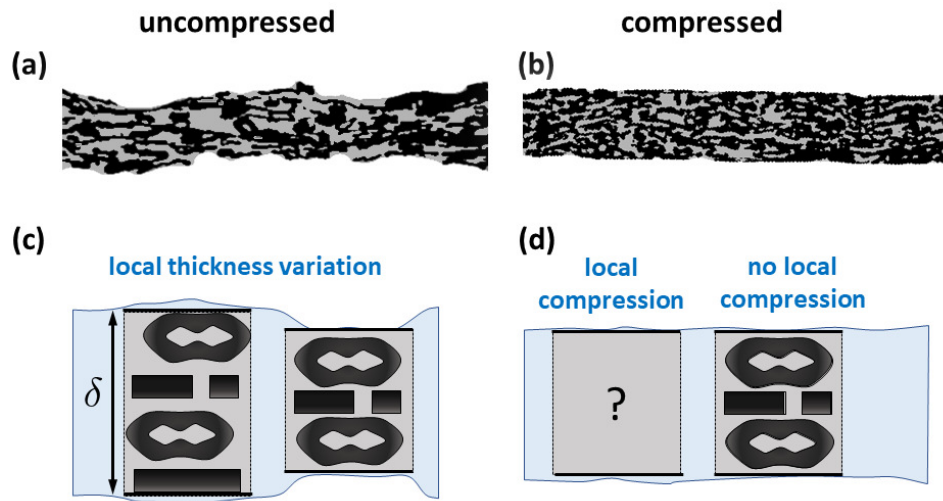


FIGURE 4. Cross sections of the binarized 3D images showing the microstructure before and after compression by hard-nip calendering (a,b). Fibers are represented in black, while the inner pores are represented in grey. The cutouts are 0.64 mm long. Schematic illustration of the local microstructure (c,d) showing local thickness variations before calendering (c) and locally varying degrees of compression after calendering (d). While thinner regions with unaltered local structure may persist, regions with a larger local basis weight will be densified. For these densified regions, symbolized by the question mark, the compression-induced change of the microstructure is a priori unknown.

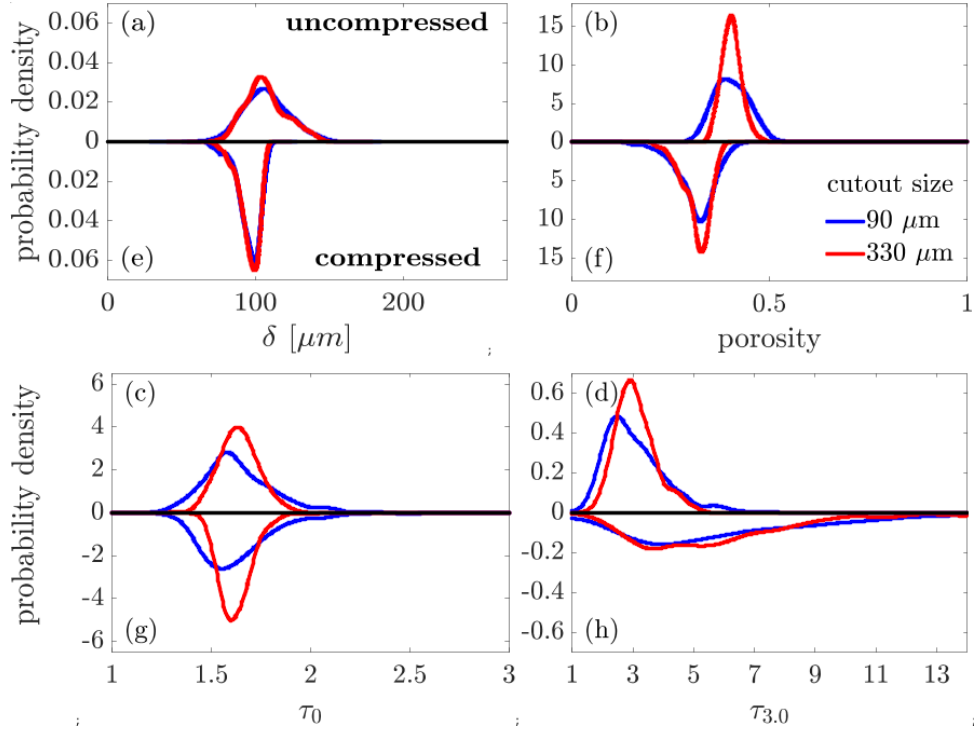


FIGURE 5. Univariate distributions of four local descriptors before and after compression for cutout lengths of  $90 \mu m$  and  $330 \mu m$ . In each panel, the probability densities in the upper panel refer to the uncompressed sample and the ones in the lower panels to the compressed sample. The descriptors considered here are local thickness (a,e), local porosity (b,f), and the local mean geodesic tortuosities  $\tau_0$  (c,g) and  $\tau_{3.0}$  (d,h).

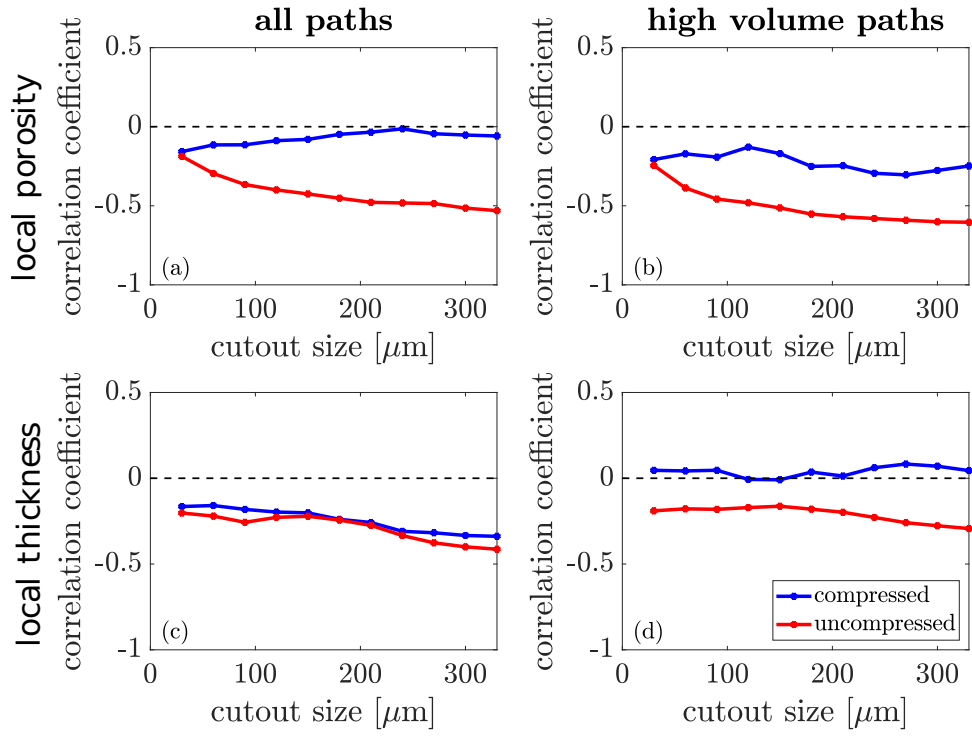


FIGURE 6. Comparison of correlation coefficients between pairs of local microstructure descriptors before and after compression. Correlation coefficients between local porosity and  $\tau_0$  (a) resp.  $\tau_{3.0}$  (b), as well as between local thickness and  $\tau_0$  (c) resp.  $\tau_{3.0}$  (d) are shown for various cutout sizes.

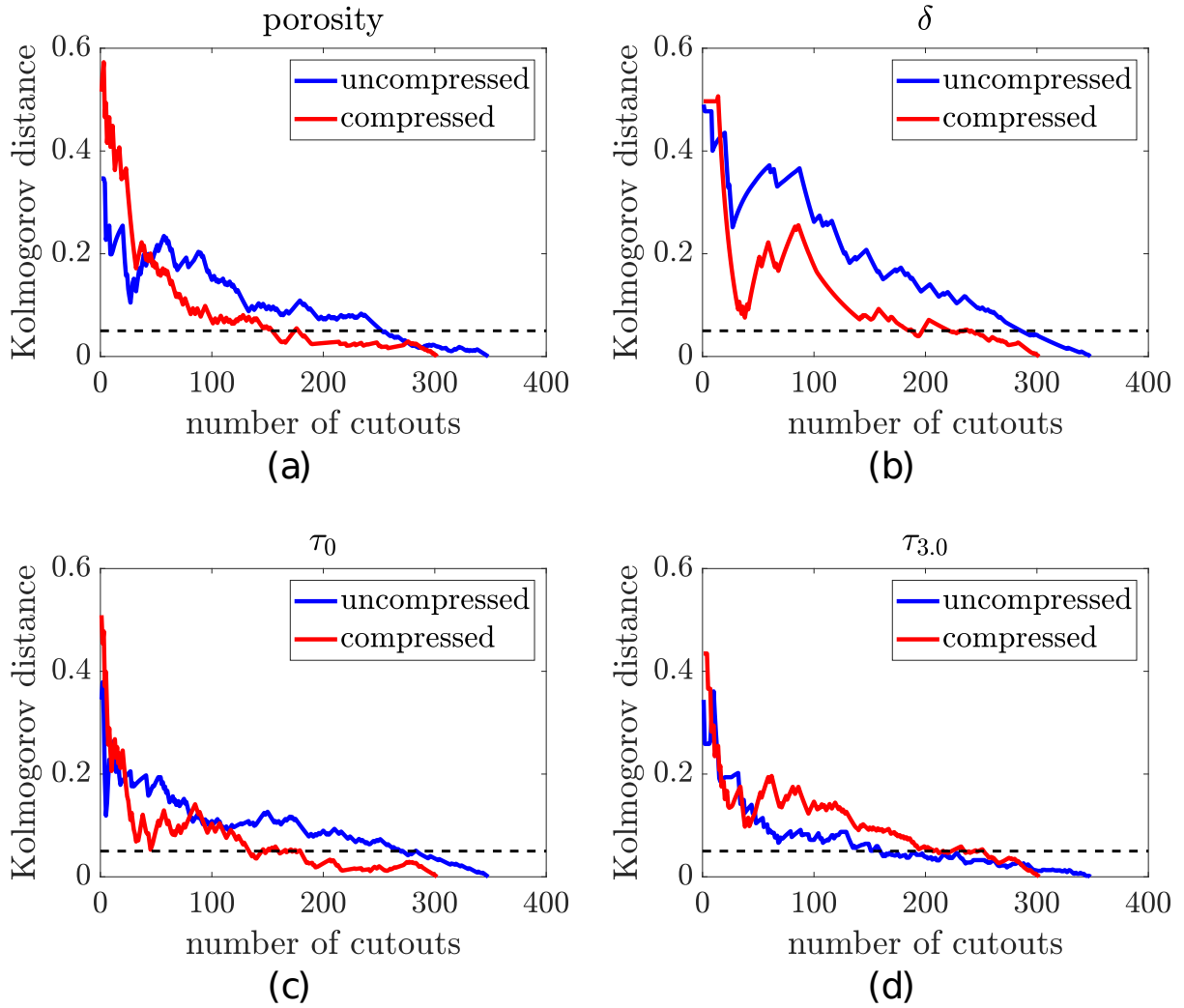


FIGURE 7. Discrepancy between the distributions of the local microstructure descriptors porosity (a), thickness  $\delta$  (b), and the path-length related descriptors  $\tau_0$  (c) and  $\tau_{3.0}$  (d) computed with all cutouts and the corresponding distribution computed with a subset of cutouts. For this purpose, a fixed cutout size of  $330 \mu m$  is considered. The  $x$ -axis indicates the number of cutouts taken into account and the discrepancy is quantified by means of the Kolmogorov distance for both, the compressed and the uncompressed sample. The black dotted lines represent the level of a Kolmogorov distance of 0.05.

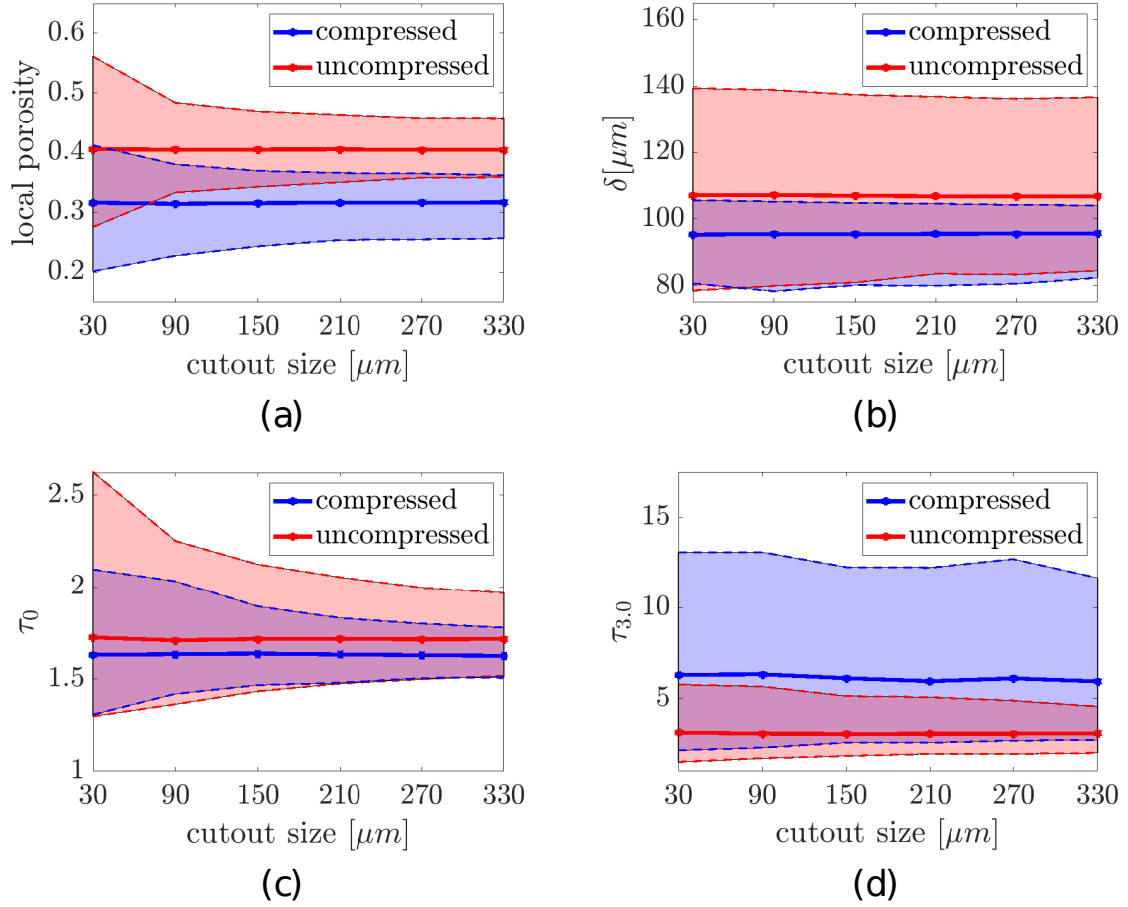


FIGURE 8. Mean values of local porosity (a), local thickness (b), local tortuosities  $\tau_0$  (c) and  $\tau_{3.0}$  (d) over the considered cutout sizes. The areas between the 0.95- and 0.05-quantiles are shaded, *i.e.*, for a given cutout size, 90 % of the corresponding local microstructure descriptors are contained in these shaded areas.

## 8. SUPPLEMENTARY MATERIAL

**$\beta$  radiographs.** Figure 9 shows two  $\beta$ -radiographs recorded for the uncompressed (a) and the compressed paper (b). The color code indicates the basis weight for each pixel in the radiograph. The mean values obtained for each sample agree well with the nominal basis weight of  $100 \text{ gm}^{-2}$  of this paper type. The variation in each of the radiographs is quantified with power spectra according to the method of Norman and Wahren (1974). The resulting spectra, given in Figure 10, show the normalized variations of the area weight as a function of the distance between two locations, denoted as wavelength. Marked variations above 10 mm indicate variations at the floc scale. At wavelengths below 1.2 mm, i.e., at distances that can be probed within the field of a view of our  $\mu$ -CT scans, also marked variations occur (Figure 10(c)). Though the variations found in the compressed (gray and black lines) and uncompressed sample (green lines) are rather similar, there is a trend to slightly larger variations in the compressed sample.

Moreover, further information regarding the influence of the cutout size on local microstructure descriptors is provided in Figures 11 and 12. These figures show the distribution of local microstructure descriptors for cutout sizes of  $30\mu\text{m}$ ,  $60\mu\text{m}$ ,  $\dots$ ,  $330\mu\text{m}$ . In particular, this additional information complements Figure 8, where mean values and quantiles of the distributions are visualized.

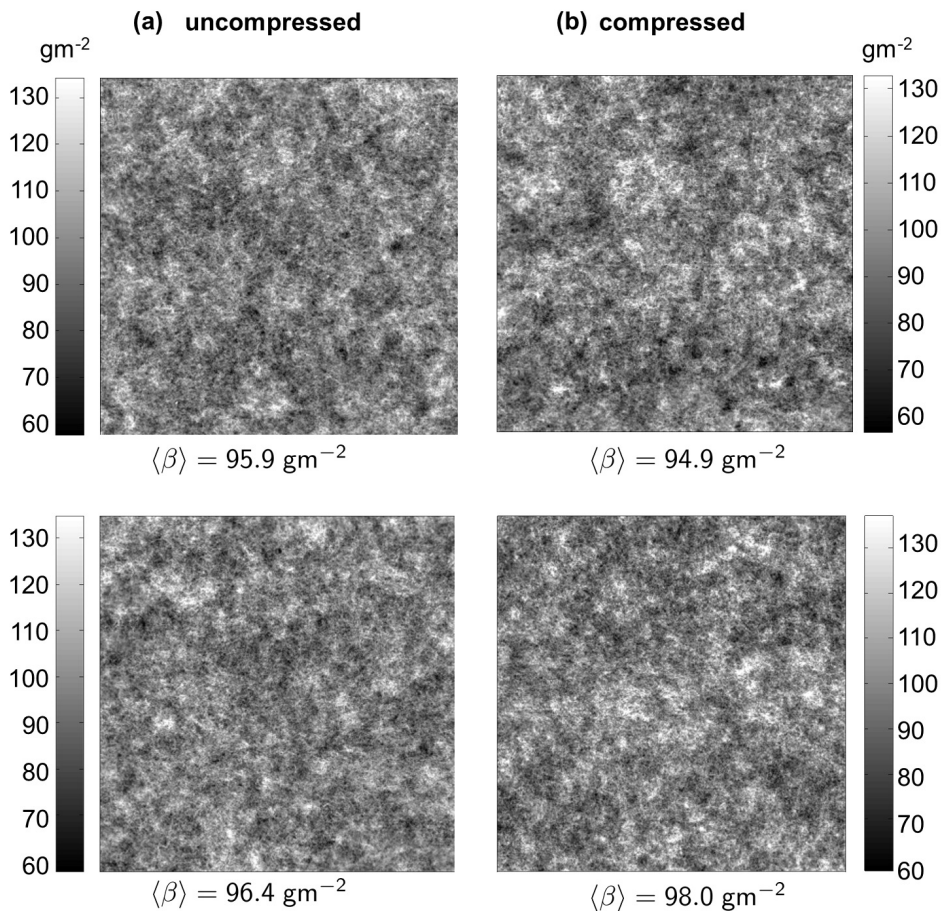


FIGURE 9.  $\beta$ -radiographs of two uncompressed (a) and two compressed samples (b) with the mean basis weight  $\langle\beta\rangle$ . Each radiograph comprises an area of  $10 \times 10 \text{ cm}^2$ . The greyscale bar indicates the local basis weight.

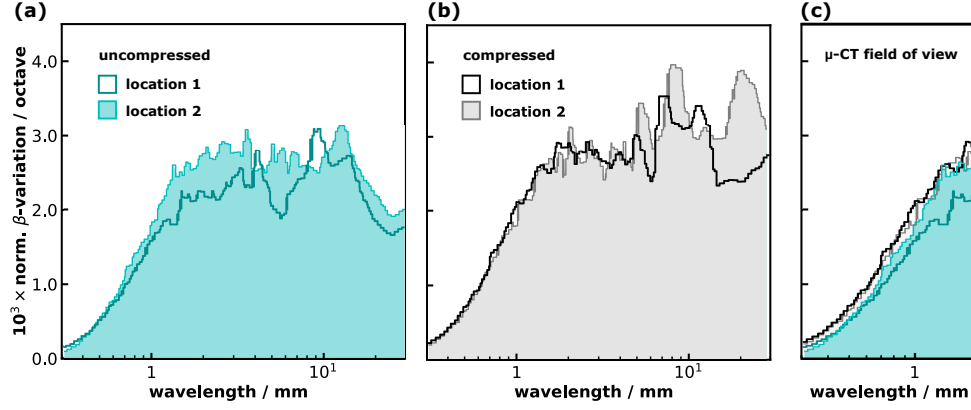


FIGURE 10. Power spectra obtained from  $\beta$ -radiographs shown in Figure 9 of the two uncompressed (a) and the two compressed samples (b). Marked normalized variations exceeding 1000/octave in  $\beta$  at wavelength above 1 cm indicate variations in the basis weight on the centimeter scale. (c) Close-up view on the power spectrum in the wavelength range monitored with the  $\mu$ -CT field of view.

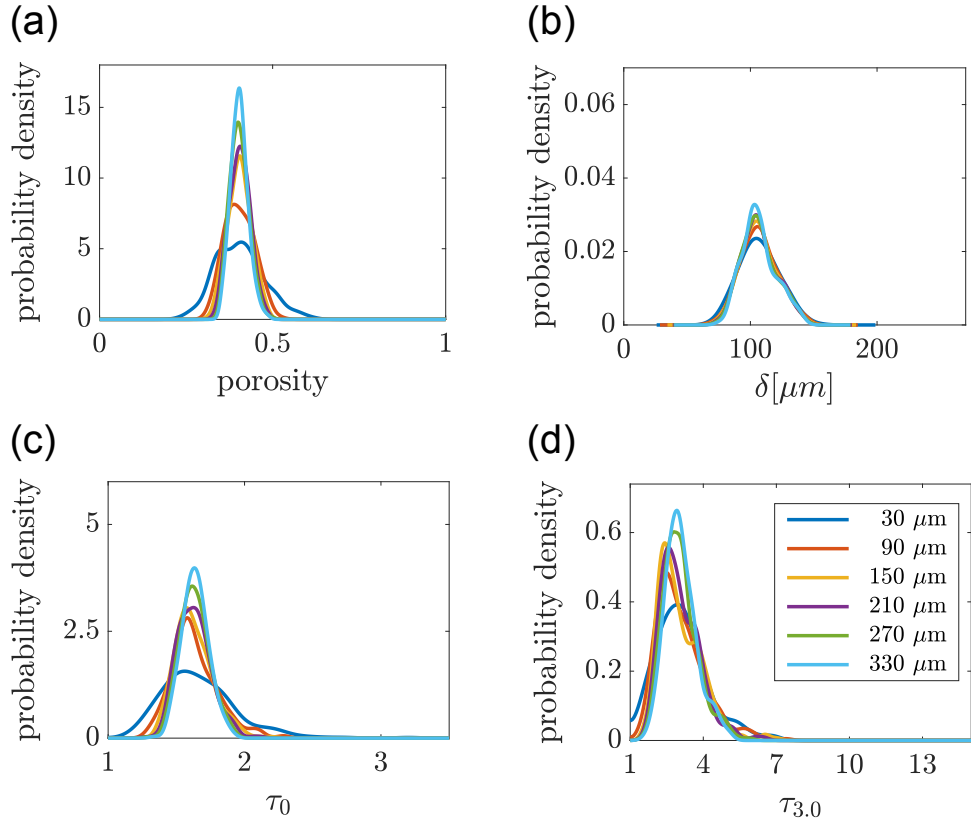


FIGURE 11. Univariate distributions of local porosity (a), local thickness (b), local tortuosities  $\tau_0$  (c) and  $\tau_{3.0}$  (d) computed from all cutouts of the uncompressed sample. The cutout sizes of 30  $\mu\text{m}$ , 90  $\mu\text{m}$ ,  $\dots$ , 330  $\mu\text{m}$  are considered.

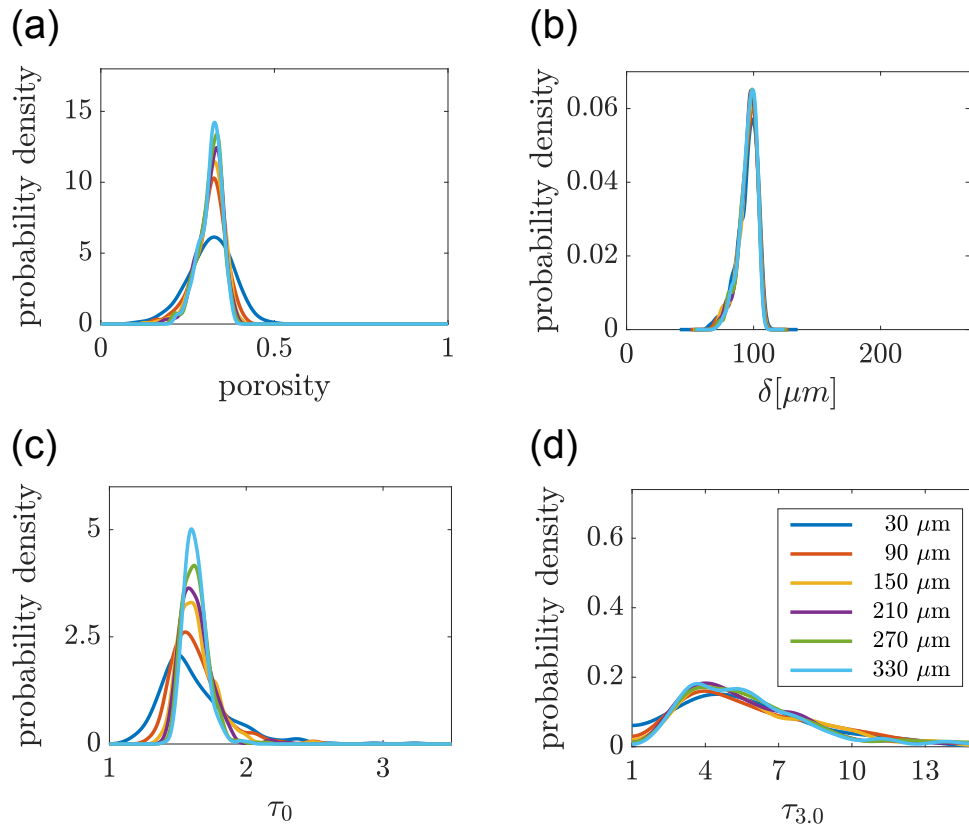


FIGURE 12. Univariate distributions of local porosity (a), local thickness (b), local tortuosities  $\tau_0$  (c) and  $\tau_{3.0}$  (d) computed from all cutouts of the compressed sample. The cutout sizes of 30  $\mu\text{m}$ , 90  $\mu\text{m}$ ,  $\dots$ , 330  $\mu\text{m}$  are considered.